NANO LETTERS
Cite This: Nano Lett. 2018, 18, 2957−2963
Letter
pubs.acs.org/NanoLett

Dual-Gated Active Metasurface at 1550 nm with Wide (>300°) Phase Tunability

Ghazaleh Kafaie Shirmanesh,[†] Ruzan Sokhoyan,[†] Ragip A. Pala,[†,§] and Harry A. Atwater*[,†,‡]

[†]Thomas J. Watson Laboratory of Applied Physics, and [‡]Kavli Nanoscience Institute, California Institute of Technology, Pasadena, California 91125, United States

Supporting Information

ABSTRACT: Active metasurfaces composed of electrically reconfigurable nanoscale subwavelength antenna arrays can enable real-time control of scattered light amplitude and phase. Achievement of widely tunable phase and amplitude in chip-based active metasurfaces operating at or near 1550 nm wavelength has considerable potential for active beam steering, dynamic hologram rendition, and realization of flat optics with reconfigurable focal lengths. Previously, electrically tunable conducting oxide-based reflectarray metasurfaces have demonstrated dynamic phase control of reflected light with a maximum phase shift of 184° (*Nano Lett.* **2016**, *16*, 5319). Here, we introduce a dual-gated reflectarray metasurface architecture that enables much wider (>300°) phase tunability. We explore light-matter interactions with dual-gated metasurface elements that incorporate two independent voltage-controlled MOS field effect channels connected in series to form a single metasurface element that enables wider phase tunability. Using indium tin oxide (ITO) as the active metasurface material and a composite hafnia/alumina gate dielectric, we demonstrate a prototype dual-gated metasurface with a continuous phase shift from 0 to 303° and a relative reflectance modulation of 89% under applied voltage bias of 6.5 V.

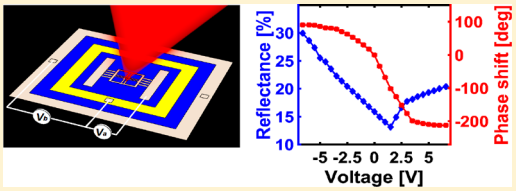

KEYWORDS: *Tunable metasurface, transparent conducting oxide, beam steering, active nanophotonics, epsilon-near-zero materials, field effect modulation*

The ability to actively control all the important constitutive properties of light (wavelength, amplitude, phase, polarization state) via interaction with tunable nanoscale elements is a grand challenge in nanophotonics. Metasurfaces are two-dimensional nanostructured surfaces that enable versatile wavefront control for scattered light.[1] Metasurfaces can also be viewed as arrays of subwavelength antennas such that each antenna imposes a predefined phase shift, amplitude change, and polarization rotation on the scattered light. The control offered by metasurfaces over the properties of reflected or transmitted light has given rise to the field of flat optics, which is exploring how metasurfaces can be used for creation of low-profile optical components.[2,3] To date, metasurfaces have been used to realize focusing mirrors,[4] focusing lenses,[5] holograms,[6−8] and polarization converters.[9,10] However, the metasurfaces in these prior reports are passive, which means their properties are fixed at the time of the fabrication, and they do not allow for postfabrication tunability. The ability to actively and dynamically tune the properties of metasurfaces would enable dynamic holograms, focusing lenses with reconfigurable focal lengths, and beam steering, a key requirement for future chip-based light detection and ranging (LIDAR) systems.

A number of approaches have been used to actively control the optical response of metasurfaces in the mid-infrared,[11−17] near-infrared,[18−25] and visible[26] wavelength ranges. The target operating wavelength usually dictates the appropriate material platform and tuning mechanism to realize actively tunable metasurfaces. In the mid-infrared wavelength range, carrier density modulation via gating of graphene,[12,13,27] GaAs[14] or indium tin oxide (ITO),[15] has been employed as a mechanism to modulate metasurface reflectance. Also, thermo-optic tuning of PbTe antennas[16] has yielded actively tunable structures in this wavelength range. A continuous phase shift from 0 to 230° by graphene gating under applied bias at a wavelength of 8.5 μm was recently reported.[11] In the near-infrared and visible wavelength range, researchers have employed a number of different physical mechanisms to realize active metasurfaces.[18−24,26,28] For example, metasurfaces with integrated liquid crystal active layers have enabled control of light transmittance by applying a direct current (dc) bias or heating the liquid crystal.[22,23] The reflectance and transmittance of a metasurface can be mechanically modulated[29] using electrostatic and magnetic forces.[19,20] Although these reports indicate options for active control of scattered light intensity, phase modulation of scattered light upon external actuation is of increasing importance.

Beam steering has been demonstrated with chip-based silicon photonics phased arrays operating at a wavelength of λ = 1550 nm.[30,31] In this approach, the phase of each antenna is actively tuned by a waveguide-based thermo-optic phase shifter through an integrated heater on the silicon chip. The silicon photonics

Received: January 25, 2018
Revised: March 6, 2018
Published: March 23, 2018

DOI: 10.1021/acs.nanolett.8b00351
Nano Lett. 2018, 18, 2957−2963

approach enables continuous tuning of the phase of emitted light from 0 to 360° upon application of external bias. However, the large pixel size of the phased array (9 μm × 9 μm) results in undesired side lobes. Moreover, thermo-optic control limited the modulation frequency of these phased arrays to less than 50 kHz,[32] which is too slow for versatile beam steering in technologically important LIDAR applications, and the thermal crosstalk between phase shifters and the photodetectors limited the detection range to 20°.[33]

Metasurfaces offer a different approach to a phased array architecture, in which the array is intrinsically two-dimensional and the subwavelength antenna dimensions and antenna spacing can suppress side lobes. Hence, it would be highly desirable to have a tunable metasurface platform for comprehensive and active control of scattered light in the near-infrared spectral range. We have previously investigated field-effect modulation of the carrier density and refractive index of heavily doped semiconductors as an approach to actively tunable near-infrared metasurfaces.[34] This approach relies on the field effect-induced charge accumulation or depletion in the semiconducting electrode of a nanoscale metal−oxide−semiconductor (MOS) structure that also serves as a resonant antenna. Using ITO as a semiconducting layer of the MOS field effect structure enabled active modulation of the optical response of plasmonic reflectarray metasurfaces[34,35] with a corresponding reflected light phase shift from 0 to 184° for an applied bias between 0 to 2.5 V. Although conceptually promising as an approach to active metasurface design, in order to realize a comprehensively tunable metasurface a phase shift from 0° approaching to 360° is desirable.

We report here the design and fabrication of dual-gated field-effect-tunable metasurface antenna arrays that enable phase shifts exceeding 300° at a wavelength of λ = 1550 nm. Our dual-gated metasurface features two charge accumulation/depletion layers within the dielectric spacer of each active metasurface antenna (Figure 1a). The dual-gated metasurface structure consists of an Al back reflector, a gate-dielectric/ITO/gate-dielectric heterostructure and a periodic array of Al nanoantennas with a "fishbone" pattern (Figures 1a, b). A scanning electron microscope (SEM) image of the antenna array is shown in Figure 1c. Each metasurface element permits application of two independent dc voltages, (i) between the ITO layer and the fishbone antenna and (ii) between the ITO layer and the back reflector. As a result, both the top and bottom ITO/gate-dielectric interfaces can exhibit the charge accumulation or depletion under applied external bias. This design facilitates a large variation of the complex refractive index of the ITO layer via carrier density modulation at both its top and bottom interfaces (Figure 1b) and is a key reason for the wide phase tunability of our dual-gated metasurface.

In designing dual-gated metasurfaces, we account for a number of considerations that can increase the metasurface tunability and efficiency. We choose the ITO carrier concentration to be N_0 = 3 × 10^{20} cm^{-3} to ensure that the real part of the dielectric permittivity of the ITO layer is positive at a wavelength of λ = 1550 nm when no external bias is applied. Under bias, a charge accumulation layer is formed in the ITO, and the real part of the dielectric permittivity of the accumulation layer can change its sign, undergoing the transition from the optically dielectric to optically metallic phase. When the dielectric permittivity of the accumulation layer is in the epsilon-near-zero (ENZ) region, which means −1 < Re(ε) < 1, the optical electric field intensity in the accumulation layer is strongly enhanced, resulting in the modulation of the intensity and phase of the scattered light.[15,36−38] The optical electric field enhancement in the ENZ region of ITO arises from the continuity of the normal component of the electric displacement as the index approaches zero in this region.[36,37] This suggests that increasing the number of the accumulation/depletion layers within the active region of the metasurface antenna is beneficial for enhancing phase tunability. On the other hand, since the optical loss of the ITO layer is non-negligible (Supporting Information Part 1), we design the ITO layer to be as thin as possible to ensure higher reflectance. On the basis of these considerations, the

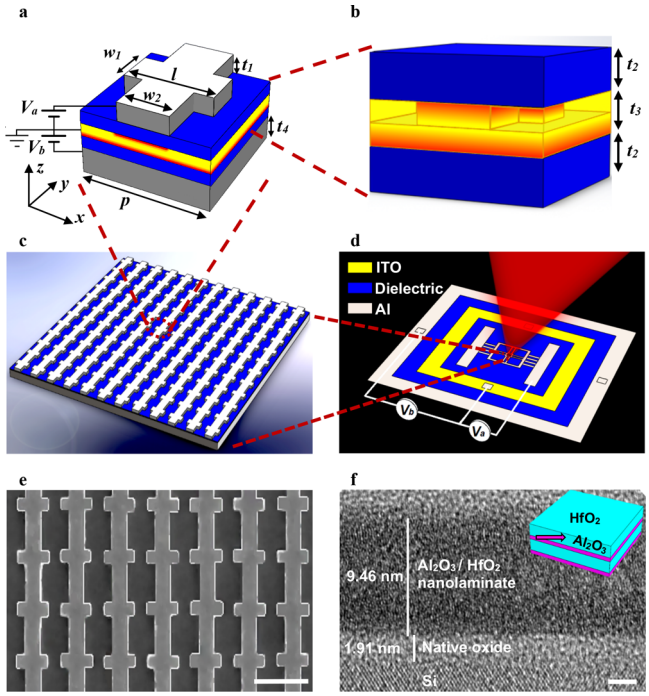

Figure 1. (a) Schematic of the unit cell of the dual-gated metasurface, which is composed of an Al back reflector, a bottom gate dielectric, an ITO layer, followed by another gate dielectric on top of which Al fishbone antennas are located. The thicknesses of the antenna array, the gate dielectrics, the ITO layer, and the back reflector are t_1= 40 nm, t_2= 9.5 nm, t_3= 5 nm, and t_4= 80 nm, respectively. The antenna dimensions are l = 280 nm and w_1 = 120 nm, and the electrode width is w_2 = 170 nm. The period of the metasurface is p = 400 nm. A voltage bias V_a is applied between the ITO layer and the top antennas, while another voltage bias V_b is applied between the Al back reflector and the ITO layer. The two applied voltage biases result in the formation of two accumulation/depletion regions in the ITO layer at the top and bottom ITO/gate-dielectric interfaces. (b) A magnified image of the dielectric spacer of the metasurface that consists of the top gate dielectric, the ITO layer, and the bottom gate dielectric. (c) Schematic of the metasurface. (d) Schematic showing the bias application configuration. The nanoantenna array is electrically connected to an external pad to which we apply the voltage. (e) Scanning electron microscope image of our metasurface. Scale bar is 500 nm. (f) Transmission electron microscope image of an Al_2O_3/HfO_2 nanolaminate, which serves as a gate dielectric in our metasurface. Scale bar is 2 nm. The Al_2O_3/HfO_2 nanolaminate is grown via atomic layer deposition (ALD). Our ALD process consists of two growth periods each including 10 cycles of Al_2O_3 and 30 cycles of HfO_2, followed by a 30 s long rapid temperature annealing treatment at 600 °C. The inset shows the deposition sequence of the nanolaminate.

DOI: 10.1021/acs.nanolett.8b00351
Nano Lett. 2018, 18, 2957−2963

ITO layer thickness is chosen to be 5 nm in our dual-gated metasurface.

Another parameter that determines the performance is the choice of the plasmonic metal. The work functions of Al and Ag, which are both near 4.3 eV, are quite close to the work function of ITO when the carrier concentration equals $N_0 = 3 \times 10^{20}$ cm^{-3}, while the work function of Au (5.1 eV) is significantly higher than that of the ITO. Hence, using Al or Ag as a metal electrode in the metal/gate-dielectric/ITO capacitor reduces the zero-bias band bending in the ITO layer compared to an Au electrode. This implies that in the case of Al or Ag electrodes, one needs to apply lower bias voltages to overcome the depletion and form an accumulation layer in the ITO at the gate-dielectric/ITO interface. Previous research has indicated that Ag can also migrate into the gate dielectric layers under applied electrical bias.[26,39] To eliminate this issue, we use Al, a CMOS-compatible material, as the plasmonic metal in our tunable metasurfaces.

The attainable optical modulation in our tunable metasurface is also determined by the choice of the gate dielectric material. To enable the largest possible variation of carrier density in ITO under applied voltage, one would ideally like to have a gate dielectric with high dc permittivity and high breakdown field. Al_2O_3 and HfO_2 are among the most commonly used high dielectric constant gate dielectric materials, employed in field-effect transistor technology. Al_2O_3 exhibits good thermal stability and almost perfect interfacial properties with Si-based substrates, has a large bandgap, and a high breakdown field of up to 10 MV/cm.[40,41] However, it suffers from a relatively low dc permittivity of $k_{Al_2O_3} = 9$. On the other hand, HfO_2 is a CMOS compatible material with a wide bandgap, and relatively high dielectric constant of up to $k_{HfO_2} = 25$. But it exhibits a small breakdown field of 3.1 MV/cm, and high leakage current induced by its low crystallization temperature. Previous research has shown that Al_2O_3/HfO_2 nanolaminates, commonly referred to as "HAOL" materials, can have superior electrostatic characteristics as compared to both Al_2O_3 and HfO_2.[42] HAOL structures, which are grown via consecutive deposition of ultrathin Al_2O_3 and HfO_2 layers, have previously shown to have the low leakage current and high breakdown field characteristics of Al_2O_3 and also the large dc permittivity characteristic of HfO_2. During our fabrication process, we grew thin HAOL films by using atomic layer deposition (ALD) and compared their properties with separately grown Al_2O_3 and HfO_2 films (for fabrication details see Supporting Information Part 2). We used transmission electron microscopy (TEM), as well as capacitance−voltage ($C-V$) and current−voltage ($I-V$) measurements to characterize the deposited films. We found that the dc permittivities of our Al_2O_3, HfO_2, and HAOL films were equal to $k_{Al_2O_3} = 10.5$, $k_{HfO_2} = 17.8$, and $k_{HAOL} = 22$, respectively. Furthermore, the measured breakdown fields of the fabricated Al_2O_3, HfO_2, and HAOL films were $E_{Al_2O_3} = 7.4$ MV/cm, $E_{HfO_2} = 3.1$ MV/cm, and $E_{HAOL} = 7.2$ MV/cm, respectively. Because HAOL structures showed superior electrostatic performance as compared to the Al_2O_3 and HfO_2 films, we used HAOL structures as the gate dielectric in our dual-gated metasurfaces.

After identifying the optimal constituent materials, we fabricated dual-gated tunable metasurfaces. First, we deposited an 80 nm-thick Al back reflector on a 100 Si wafer by electron beam evaporation. Next, we grew a 9.5 nm-thick Al_2O_3/HfO_2 nanolaminate via ALD, and sputtered a 5 nm-thick layer of ITO. We chose the ITO carrier concentration to be $N_0 = 3 \times 10^{20}$ cm^{-3}. To characterize our ITO films, we performed Hall measurements and spectroscopic ellipsometry on 5 nm-thick ITO layers deposited on quartz and Si substrates, respectively. Once we deposited the ITO layer, we deposited the top gate dielectric, consisting of a 9.5 nm-thick HAOL layer. Finally, we fabricated a 40 nm-thick Al fishbone antenna array on top of the upper HAOL layer by electron beam evaporation of Al and patterning by electron beam lithography. The antenna width and length were w_1= 120 nm and l = 280 nm, and the width of the stripe electrode was w_2= 170 nm (Figure 1a). During fabrication, our samples were patterned to allow for easy application of a bias between the Al back reflector and the ITO layer (V_b in Figure 1d). The Al fishbone antennas were connected to an external Al pad that allows for facile bias application between the fishbone antennas and the ITO layer (V_a Figure 1d). The electrode pads were then wire bonded to a compact chip carrier and circuit board for electrical gating. Figure 1d shows the bias configuration for dual-gated metasurfaces.

Electromagnetic Simulations of Dual-Gated Metasurfaces. We modeled the optical response of our metasurface under applied bias using finite difference time domain simulations coupled to device physics simulations. The device physics simulations were used to determine the charge carrier distribution in the ITO layer under applied bias. We then related the calculated carrier density to the complex dielectric permittivity of ITO ε_{ITO} using a Drude model approach: $\varepsilon_{ITO} = \varepsilon_\infty - \omega_p^2/(\omega^2 + i\omega\gamma)$, because the plasma frequency ω_p is proportional to the square root of the carrier density of ITO (N_{ITO}). Here, γ is the damping constant and ε_∞ is a fitting constant. ω_p, γ, and ε_∞ at zero bias are determined empirically from Hall measurements and ellipsometry (Supporting Information Part 3). ω is the angular frequency, which is related to the wavelength λ as $\lambda = 2\pi c/\omega$, where c is the speed of light in vacuum.

The electrostatic performance of the dual-gated tunable metasurface element can be viewed as two parallel plate capacitor structures which are connected in series. Therefore, two independent bias voltages can be applied to each metasurface element, V_a and V_b (Figure 1a). In what follows we assume that $|V_a| = |V_b|$ that now yields two accessible regimes of device operation, where $\text{sign}(V_a \times V_b) \geq 0$ (Case I) and where $\text{sign}(V_a \times V_b) \leq 0$ (Case II). In other words, in Case I there is a simultaneous charge accumulation or simultaneous charge depletion at both ITO layer interfaces (Figure 2a,c,e). In Case II, charge accumulation at the top ITO/HAOL interface is accompanied by charge depletion at the bottom ITO/HAOL interface or, vice versa, charge depletion at the top ITO/HAOL interface is accompanied by charge accumulation at the bottom ITO/HAOL interface (Figure 2b,d,f). The charge carrier distributions in the 5 nm-thick ITO layer for Case I and Case II are depicted in Figure 2c,d, respectively. Here, the z-position varies between 0 and 5 nm with 0 corresponding to the bottom ITO/HAOL interface and 5 nm corresponding to the top ITO/HAOL interface.

We note that only the portion of the ITO located directly beneath the Al fishbone antenna is optically modulated at the top ITO/HAOL interface (Figure 1b). As seen in Figure 2c, in Case I the ITO dielectric permittivity at the bottom ITO/HAOL interface is always equal to the dielectric permittivity of the ITO at the top ITO/HAOL interface beneath the fishbone

DOI: 10.1021/acs.nanolett.8b00351
Nano Lett. 2018, 18, 2957−2963

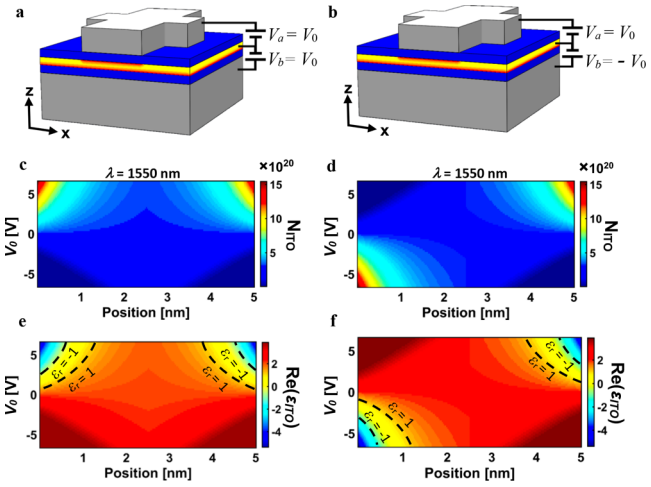

Figure 2. (a) Schematic of Case I in which there is a simultaneous charge accumulation or simultaneous charge depletion at both ITO/HAOL interfaces of the ITO layer. In Case I, we assume $V_a = V_0$ and $V_b = V_0$. (b) Schematic of Case II in which the charge accumulation (depletion) at the top ITO/HAOL interface is always accompanied by the charge depletion (accumulation) at the bottom ITO/HAOL interface. In Case II, we assume $V_a = V_0$ and $V_b = -V_0$. The charge carrier distribution in the ITO layer as a function of applied voltage V_0 for (c) Case I and (d) Case II. The real part of the dielectric permittivity of the ITO layer as a function of the applied voltage and position for (e) Case I and (f) Case II at a wavelength of λ = 1550 nm. The boundaries of the ENZ regions are marked by dashed curves.

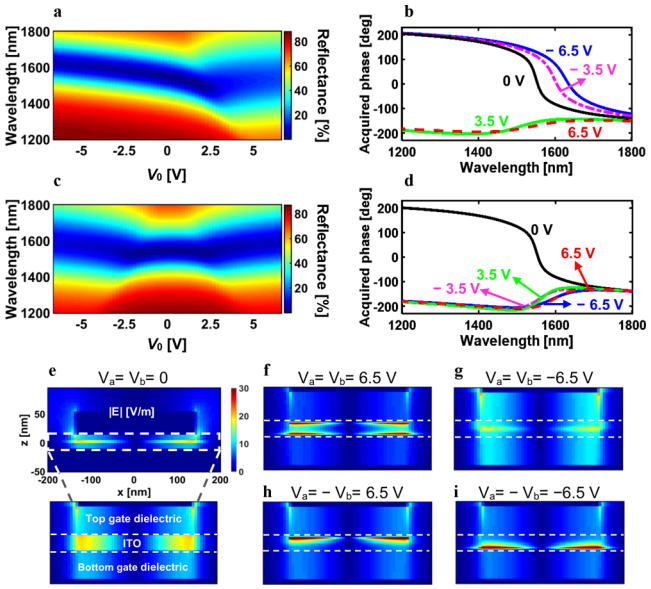

Figure 3. (a) Reflectance from the metasurface as a function of wavelength and applied voltage in Case I. (b) Phase spectrum of the reflected light for different applied voltages in Case I. (c) Reflectance as a function of wavelength and applied bias in Case II. (d) Phase spectrum for different applied voltages in Case II. (e) Spatial distribution of the magnitude of the electric field inside the metasurface element at no applied bias. The bottom part of (e) shows the magnified image of the field distribution in the HAOL/ITO/HAOL dielectric spacer of the metasurface. The close-up of the distribution of the electric field magnitude in the dielectric spacer of the metasurface when (f) V_0 = 6.5 V in Case I, (g) V_0 = −6.5 V in Case I, (h) V_0 = 6.5 V in Case II, (i) V_0 = −6.5 V in Case II.

antenna. This, however, is not true for Case II. In Case II, for sufficiently large applied voltage magnitude, there is always charge accumulation at either top or bottom interface of the ITO layer (Figure 2d).

After modeling the complex dielectric permittivity of ITO as a function of position and applied voltage, we calculated the metasurface optical response for different applied biases under normal incidence illumination with a transverse magnetic (TM) polarized plane wave (**E**-field along *x*-direction). Figure 3a shows the dual-gated metasurface reflectance in Case I as a function of wavelength and applied voltage. In this case, a large reflectance modulation and large phase shift (Figure 3b) are observed at positive biases, when the dielectric permittivity of both the top and bottom ITO interfaces crosses into the ENZ region. The phase shift is defined as a difference between the phases of the reflected and incoming plane waves calculated at the same spatial point. In Case I, we observe a blue shift of the resonance when the applied bias increases from 0 to 2.5 V. For applied voltages larger than 2.5 V, the resonance redshifts. This is consistent with previously reported results.[34] In Case II, we observe a significant reflectance and phase modulation both at positive and negative biases (Figure 3c,d). Moreover, we observe that in Case II the reflectance spectrum is invariant with respect to the transformation $V_0 \rightarrow -V_0$. This is because in Case II both at positive and negative biases the gap plasmon resonance couples to the ENZ region in ITO that is formed in either the top or the bottom ITO layer interface.

To gain further insight, we plotted the distribution of the absolute value of the optical electric field in the metasurface element for the resonant wavelength of λ = 1550 nm (Figure 3e–i). Figure 3e shows the spatial distribution of the optical electric field at zero bias. The bottom part of Figure 3e shows the magnified region of the dielectric spacer at zero bias. When a dc bias is applied, we observe a significant variation of the distribution of the optical electric field. Figure 3f shows the optical electric field distribution in Case I at an applied voltage of V_0 = 6.5 V. As seen in Figure 3f, the optical electric field is enhanced at both the top and bottom ITO/HAOL interfaces due to the ENZ regions that are formed at these interfaces (Figure 2e). On the other hand, when the applied dc bias in Case I is equal to V_0 = −6.5 V, the ITO layer is depleted at both top and bottom interfaces (Figure 2c–e) and therefore we do not observe a significant optical field enhancement in the ITO layer (Figure 3g). In Case II, however, a dramatic optical field enhancement is observed at both positive and negative applied biases $V_0 = \pm 6.5$ V (Figure 3h,i). In this case at an applied bias of V_0 = 6.5 V, we observe the optical electric field enhancement in the ITO layer around the top ITO/HAOL interface due to the ENZ region formed in the ITO layer (Figure 3h). Similarly, Figure 3i shows that in Case II, the optical electric field is enhanced around the bottom part of the ITO layer, when the applied bias is equal to V_0 = −6.5 V (for further field profiles, see Supporting Information Part 4). The analysis of the optical field profile suggests that strong light confinement in the dielectric gap of the plasmonic antenna significantly contributes to the observed optical modulation.

Figure 3b,d illustrates how dual-gated metasurfaces significantly alter the phase of the reflected light under an applied bias. In Figure 4, we plot the phase shift and reflectance as a function of applied bias V_0 at a wavelength of λ = 1550 nm. Figure 4a, which corresponds to Case I, shows that this bias configuration gives a continuously tunable phase shift between 70° and −245°, when the applied voltage is varied between V_0 = −6.5 V and V_0 = 6.5 V. This amounts to a total tunable phase

DOI: 10.1021/acs.nanolett.8b00351
Nano Lett. 2018, 18, 2957–2963

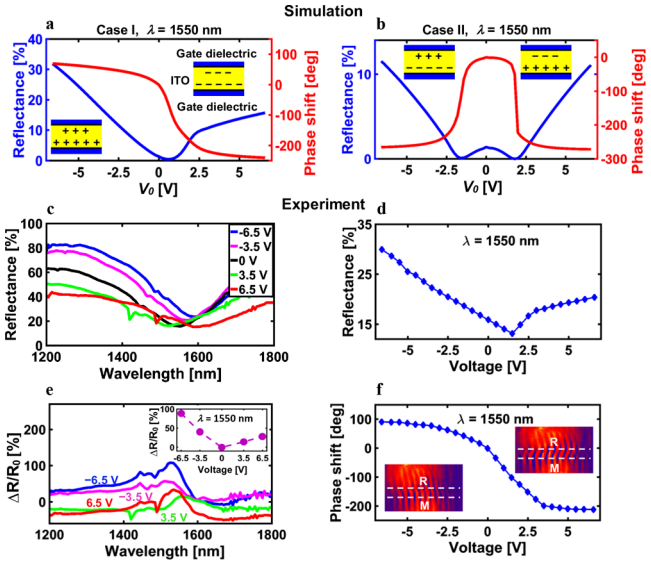

Figure 4. (a,b) Simulated reflectance and phase shift of the metasurface as a function of voltage V_0. The wavelength is fixed at λ = 1550 nm. The panel (a) corresponds to Case I, in which there is a simultaneous charge accumulation or simultaneous charge depletion in the ITO layer at the both ITO/HAOL interfaces. The panel (b) corresponds to Case II in which the charge accumulation at the top ITO/HAOL interface is always accompanied by the charge depletion at the bottom ITO/HAOL interface and vice versa. The insets of (a,b) schematically show the charge distribution in the dielectric spacer of the metasurface. (c) Measured reflectance spectra in Case I at different applied voltages V_0. (d) Measured reflectance in Case I as a function of applied bias V_0 and at the fixed wavelength of λ = 1550 nm. (e) The spectra of the relative reflectance modulation $\Delta R/R_0$ for different applied voltages V_0. The inset shows the relative reflectance change at a wavelength of λ = 1550 nm as a function of applied bias V_0. (f) Measured phase shift of the metasurface as a function of applied voltage V_0 at a wavelength of λ = 1550 nm. The insets of (f) show the interference fringes at −6.5 V and +6.5 V. The dashed lines labeled as **R** and **M** indicate the interference fringes from the reference and metasurface, respectively.

shift of 315° derived from Case I. As expected, a phase shift derived from Case II is invariant with respect to the transformation $V_0 \rightarrow -V_0$ (Figure 4b). In Case II, the phase shift smoothly varies between 0 and −275°, when the applied voltage is increased from V_0 = 0 V to V_0 = 6.5 V. Thus, via an appropriate bias application, the proposed dual-gated tunable metasurface allows us to attain a tunable phase shift of 345°.

Experimental Results. Having identified an approach to metasurface design, we fabricated and characterized the tunable optical response of dual-gated metasurfaces (for fabrication details and measurement setups see Supporting Information Parts 5−7). Optical measurements were performed by illuminating our metasurfaces with linearly polarized light with incident electric field aligned with the fishbone antenna (*x*-direction in Figure 1a). In our experiments, the bias configuration corresponds to Case I, when $V_a = V_0$ and $V_b = V_0$ (Figure 2a). Figure 4c displays the measured reflectance spectra at different values of applied voltage V_0. The resonance is observed to blue shift with increasing voltage from V_0 = 0 V to V_0 = 2.5 V. When we increased the applied voltage from V_0 = 2.5 V to V_0 = 6.5 V, the resonance was observed to red shift, and likewise when we decreased the applied bias from V_0 = 0 V to V_0 = −6.5 V, a resonance red shift was observed. These observations are consistent with our simulation results (Figure 3a), which indicate that at an applied voltage of V_0 = 2.5 V we reach the ENZ region in the ITO accumulation layer, corresponding to the transition from resonance blue shift to red shift.

Figure 4d displays the reflectance as a function of applied voltage V_0 at a wavelength of λ = 1550 nm. We observe a decrease in reflectance when the applied voltage increases from V_0 = −6.5 V to V_0 = 0.6 V. Once the applied bias has passed V_0 = 0.6 V, we observe an increase in reflectance (Figure 4d). Figure 4e shows relative reflectance spectra $\Delta R/R_0 = [R(V_0) - R(0)]/R(0)$ at different applied voltage values V_0. Even though the measured reflectance modulation $\Delta R/R_0$ is fairly broadband, we observe an enhancement in $\Delta R/R_0$ around the metasurface resonant wavelength. The inset of Figure 4e shows the relative reflectance modulation $\Delta R/R_0$ as a function of applied bias V_0 at a wavelength of λ = 1550 nm. At a wavelength of λ = 1550 nm, the relative reflectance modulation is much more significant for negative rather than positive bias voltages. When V_0 decreases from V_0 = 0 V to V_0 = −6.5 V, we observe a relative reflectance modulation of 89% at a wavelength of λ = 1550 nm. On the other hand, when applied voltage V_0 increases from V_0 = 0 V to V_0 = 6.5 V, the observe that the relative reflectance modulation is only 28% (see the inset of Figure 4e). This implies that at the resonance wavelength, the formation of multiple ITO charge depletion layers influences the reflectance more significantly than the formation of multiple charge accumulation layers. This change in reflectance can be explained by the modulation of the optical electric field in the ITO layer under applied bias. At V_0 = 0 V, the formation of the magnetic dipole leads to strong absorption in the ITO layer, whereas the applied bias effectively modulates the optical field distribution in the dielectric spacer of the metasurface and leads to higher reflectance.

After performing metasurface gate-tunable reflectance measurements and identifying the resonance wavelength, we measured the phase shift of the reflected light under applied bias. For our phase shift measurements, we employed a Michelson interferometer-type (Supporting Information Part 7). In our interferometer, laser light illuminated the edge of the metasurface. Therefore, a part of the incoming beam was reflected from the metasurface, while the other part was reflected from the surrounding planar Al/HAOL/ITO/HAOL heterostructure, which acted as a built-in phase reference. The images of the formed interference fringes were recorded by a charge-coupled device camera and subsequently were processed and fitted. Our fitting procedure enabled us to retrieve the relative displacement of the interference fringes originating from the metasurface and the reference when we applied a bias.

The measured interference fringe displacement was converted into a relative phase shift (Supporting Information Part 7). Our interferometry enabled accurate phase measurements, because in this configuration errors caused by vibrations and other motion instabilities were eliminated. Examples of interference fringe images recorded at bias voltages of V_0 = −6.5 V and V_0 = +6.5 V are shown in the inset of Figure 4f. In this measurement, the laser illumination wavelength is λ = 1550 nm. The dashed white lines show the interference fringes from the metasurface (**M**) and the reference (**R**). Figure 4f shows the measured phase shift as a function of applied voltage V_0 (λ = 1550 nm). When we increased the applied voltage from V_0 = 0 V to V_0 = +6.5 V, we observed a phase shift of −211.9°, which is accompanied by a modest relative reflectance modulation of 28%. When we decreased the applied voltage from V_0 = 0 V to

DOI: 10.1021/acs.nanolett.8b00351
Nano Lett. 2018, 18, 2957−2963

V_0 = −6.5 V, we measured a phase shift of +91° that is consistent with our simulation results shown in Figure 4a. Interestingly, despite the modest phase shift recorded at negative biases $V_0 < 0$, the reflectance measured at a wavelength λ = 1550 nm increases from 13% to 30%. An overall phase shift of 303° was produced as the applied bias to the dual-gated metasurface was varied between V_0 = −6.5 V and V_0 = +6.5 V.

In summary, we have designed and fabricated a dual-gated plasmonic reflectarray metasurface that shows wide phase tunability with applied bias at a wavelength of λ = 1550 nm, and the phase of the reflected light can be continuously tuned from 0 to 303°. We have also measured a relative reflectance modulation of 89%. This large optical tunability is achieved both due to the materials employed here and to the dual-gated metasurface architecture. Each element of our dual-gated metasurfaces can be viewed as two series-connected MOS field effect structures to which two independent bias voltages can be applied, yielding a wider phase tuning range compared to a single-gated metasurface (Supporting Information Part 8). Interestingly, in our case a given phase shift can be achieved via multiple different bias configurations that yield different reflectance values, enabling an approach for reflectance modulation at a constant phase. This feature may be very useful for design and demonstration of future dynamically reconfigurable low-profile optical components such as focusing lenses with reconfigurable focal lengths, dynamic holograms, and beam steering devices.

■ ASSOCIATED CONTENT

Supporting Information

The Supporting Information is available free of charge on the ACS Publications website at DOI: 10.1021/acs.nanolett.8b00351.

Additional information, tables, and figures (PDF)

■ AUTHOR INFORMATION

Corresponding Author

*E-mail: haa@caltech.edu.

ORCID

Ghazaleh Kafaie Shirmanesh: 0000-0003-1666-3215

Ruzan Sokhoyan: 0000-0003-4599-6350

Harry A. Atwater: 0000-0001-9435-0201

Present Address

§(R.A.P.) Metamaterial Technologies Inc. 5880 W. Las Positas Blvd, Ste 51, Pleasanton, CA 94588, United States.

Notes

The authors declare no competing financial interest.

■ ACKNOWLEDGMENTS

This work was supported by Samsung Electronics (G.K.S., R.S., and H.A.A.) and the Air Force Office of Scientific Research under Grant FA9550-16-1-0019 (R.A.P.). The authors used facilities supported by the Kavli Nanoscience Institute (KNI) and Joint Center for Artificial Photosynthesis (JCAP) at Caltech. The authors would like to thank Carol Garland for help with the TEM imaging. The authors gratefully acknowledge useful discussions with Dr. Yao-Wei Huang, Dr. Pin Chieh Wu, and Dr. Duhyun Lee. The authors also gratefully acknowledge Erin Burkett and Christina Burch from the Hixon Writing Center at Caltech for providing feedback and guidance on writing the manuscript.

■ REFERENCES

(1) Yu, N.; Genevet, P.; Kats, M. A.; Aieta, F.; Tetienne, J.-P.; Capasso, F.; Gaburro, Z. *Science* **2011**, *334*, 333−337.

(2) Yu, N.; Capasso, F. *Nat. Mater.* **2014**, *13*, 139−150.

(3) Arbabi, A.; Horie, Y.; Bagheri, M.; Faraon, A. *Nat. Nanotechnol.* **2015**, *10*, 937−943.

(4) Pors, A.; Nielsen, M. G.; Eriksen, R. L.; Bozhevolnyi, S. I. *Nano Lett.* **2013**, *13*, 829−834.

(5) Khorasaninejad, M.; Chen, W. T.; Devlin, R. C.; Oh, J.; Zhu, A. Y.; Capasso, F. *Science* **2016**, *352*, 1190−1194.

(6) Huang, Y.-W.; Chen, W. T.; Tsai, W.-Y.; Wu, P. C.; Wang, C.-M.; Sun, G.; Tsai, D. P. *Nano Lett.* **2015**, *15*, 3122−3127.

(7) Zheng, G.; Muhlenbernd, H.; Kenney, M.; Li, G.; Zentgraf, T.; Zhang, S. *Nat. Nanotechnol.* **2015**, *10*, 308−312.

(8) Chen, W. T.; Yang, K.-Y.; Wang, C.-M.; Huang, Y.-W.; Sun, G.; Chiang, I.-D.; Liao, C. Y.; Hsu, W.-L.; Lin, H. T.; Sun, S.; et al. *Nano Lett.* **2014**, *14*, 225−230.

(9) Black, L.-J.; Wang, Y.; de Groot, C. H.; Arbouet, A.; Muskens, O. L. *ACS Nano* **2014**, *8*, 6390−6399.

(10) Wu, P. C.; Tsai, W.-Y.; Chen, W. T.; Huang, Y.-W.; Chen, T.-Y.; Chen, J.-W.; Liao, C. Y.; Chu, C. H.; Sun, G.; Tsai, D. P. *Nano Lett.* **2017**, *17*, 445−452.

(11) Sherrott, M. C.; Hon, P. W. C.; Fountaine, K. T.; Garcia, J. C.; Ponti, S. M.; Brar, V. W.; Sweatlock, L. A.; Atwater, H. A. *Nano Lett.* **2017**, *17*, 3027−3034.

(12) Dabidian, N.; Kholmanov, I.; Khanikaev, A. B.; Tatar, K.; Trendafilov, S.; Mousavi, S. H.; Magnuson, C.; Ruoff, R. S.; Shvets, G. *ACS Photonics* **2015**, *2*, 216−227.

(13) Yao, Y.; Kats, M. A.; Genevet, P.; Yu, N.; Song, Y.; Kong, J.; Capasso, F. *Nano Lett.* **2013**, *13*, 1257−1264.

(14) Jun, Y. C.; Reno, J.; Ribaudo, T.; Shaner, E.; Greffet, J.-J.; Vassant, S.; Marquier, F.; Sinclair, M.; Brener, I. *Nano Lett.* **2013**, *13*, 5391−5396.

(15) Park, J.; Kang, J.-H.; Liu, X.; Brongersma, M. L. *Sci. Rep.* **2015**, *5*, 15754.

(16) Lewi, T.; Evans, H. A.; Butakov, N. A.; Schuller, J. A. *Nano Lett.* **2017**, *17*, 3940−3945.

(17) Iyer, P. P.; Pendharkar, M.; Palmstrom, C. J.; Schuller, J. A. *Nat. Commun.* **2017**, *8*, 472.

(18) Cencillo-Abad, P.; Ou, J.-Y.; Plum, E.; Valente, J.; Zheludev, N. I. *Nanotechnology* **2016**, *27*, 485206.

(19) Ou, J.-Y.; Plum, E.; Zhang, J.; Zheludev, N. I. *Nat. Nanotechnol.* **2013**, *8*, 252−255.

(20) Valente, J.; Ou, J.-Y.; Plum, E.; Youngs, I. J.; Zheludev, N. I. *Nat. Commun.* **2015**, *6*, 7021.

(21) Zhu, Z. H.; Evans, P. G.; Haglund, R. F.; Valentine, J. G. *Nano Lett.* **2017**, *17*, 4881−4885.

(22) Decker, M.; Kremers, C.; Minovich, A.; Staude, I.; Miroshnichenko, A. E.; Chigrin, D.; Neshev, D. N.; Jagadish, C.; Kivshar, Y. S. *Opt. Express* **2013**, *21*, 8879−8885.

(23) Sautter, J.; Staude, I.; Decker, M.; Rusak, E.; Neshev, D. N.; Brener, I.; Kivshar, Y. S. *ACS Nano* **2015**, *9*, 4308−4315.

(24) Olivieri, A.; Chen, C.; Hassan, S.; Lisicka-Skrzek, E.; Tait, R. N.; Berini, P. *Nano Lett.* **2015**, *15*, 2304−2311.

(25) de Galarreta, C. R.; Alexeev, A. M.; Au, Y.-Y.; Lopez-Garcia, M.; Klemm, M.; Cryan, M.; Bertolotti, J.; Wright, C. D. *Adv. Funct. Mater.* **2018**, *28*, 1704993.

(26) Thyagarajan, K.; Sokhoyan, R.; Zornberg, L.; Atwater, H. A. *Adv. Mater.* **2017**, *29*, 1701044.

(27) Wu, P. C.; Papasimakis, N.; Tsai, D. P. *Phys. Rev. Appl.* **2016**, *6*, 044019.

(28) Chu, C. H.; Tseng, M. L.; Chen, J.; Wu, P. C.; Chen, Y.-H.; Wang, H.-C.; Chen, T.-Y.; Hsieh, W. T.; Wu, H. J.; Sun, G.; Tsai, D. P. *Laser Photonics Rev.* **2016**, *10*, 1063−1063.

(29) Ee, H.-S.; Agarwal, R. *Nano Lett.* **2016**, *16*, 2818−2823.

(30) Heck, M. J. R. *Nanophotonics* **2017**, *6*, 93−107.

(31) Sun, J.; Timurdogan, E.; Yaacobi, A.; Hosseini, E. S.; Watts, M. R. *Nature* **2013**, *493*, 195−199.

DOI: 10.1021/acs.nanolett.8b00351
Nano Lett. 2018, 18, 2957−2963

(32) Yaacobi, A.; Sun, J.; Moresco, M.; Leake, G.; Coolbaugh, D.; Watts, M. R. *Opt. Lett.* **2014**, *39*, 4575−4578.
(33) Poulton, C. V.; Yaacobi, A.; Cole, D. B.; Byrd, M. J.; Raval, M.; Vermeulen, D.; Watts, M. R. *Opt. Lett.* **2017**, *42*, 4091−4094.
(34) Huang, Y.-W.; Lee, H. W. H.; Sokhoyan, R.; Pala, R. A.; Thyagarajan, K.; Han, S.; Tsai, D. P.; Atwater, H. A. *Nano Lett.* **2016**, *16*, 5319−5325.
(35) Park, J.; Kang, J.-H.; Kim, S. J.; Liu, X.; Brongersma, M. L. *Nano Lett.* **2017**, *17*, 407−413.
(36) Lee, H. W.; Papadakis, G.; Burgos, S. P.; Chander, K.; Kriesch, A.; Pala, R.; Peschel, U.; Atwater, H. A. *Nano Lett.* **2014**, *14*, 6463−6468.
(37) Vasudev, A. P.; Kang, J.-H.; Park, J.; Liu, X.; Brongersma, M. L. *Opt. Express* **2013**, *21*, 26387−26397.
(38) Lu, Z.; Zhao, W.; Shi, K. *IEEE Photonics J.* **2012**, *4*, 735−740.
(39) Lee, J.; Lu, W. D. *Adv. Mater.* **2018**, *30*, 1702770.
(40) Ye, P. D.; Yang, B.; Ng, K. K.; Bude, J.; Wilk, G. D.; Halder, S.; Hwang, J. C. M. *Appl. Phys. Lett.* **2005**, *86*, 063501.
(41) Hinkle, C. L.; Sonnet, A. M.; Vogel, E. M.; McDonnell, S. *Appl. Phys. Lett.* **2008**, *92*, 071901.
(42) Cao, D.; Cheng, X.; Zheng, L.; Xu, D.; Wang, Z.; Xia, C.; Shen, L.; Yu, Y.; Shen, D. *J. Vac. Sci. Technol., B: Nanotechnol. Microelectron.: Mater., Process., Meas., Phenom.* **2015**, *33*, 01A101.

DOI: 10.1021/acs.nanolett.8b00351
Nano Lett. 2018, 18, 2957−2963